

Geophysical Research Letters[®]



RESEARCH LETTER

10.1029/2021GL095459

Tracking Crustal Permeability and Hydrothermal Response During Seafloor Eruptions at the East Pacific Rise, 9°50'N

T. Barreyre^{1,2} , R. Parnell-Turner³ , J.-N. Wu³ , and D. J. Fornari² 

¹Department of Earth Science - Center for Deep Sea Research, University of Bergen, Bergen, Norway, ²Geology and Geophysics Department, Woods Hole Oceanographic Institution, Woods Hole, MA, USA, ³Institute of Geophysics and Planetary Physics, Scripps Institution of Oceanography, University of California San Diego, La Jolla, CA, USA

Key Points:

- Hydrothermal vent fluid temperature data modeled with ocean tides reveal permeability changes associated with seafloor volcanic eruptions
- Changes in crustal permeability caused by magmatic intrusion and volcanic eruption control first-order hydrothermal circulation processes
- This methodology expands the potential of forecasting seafloor eruptions along the global mid-ocean ridge network

Supporting Information:

Supporting Information may be found in the online version of this article.

Correspondence to:

T. Barreyre,
thibaut.barreyre@uib.no

Citation:

Barreyre, T., Parnell-Turner, R., Wu, J.-N., & Fornari, D. J. (2022). Tracking crustal permeability and hydrothermal response during seafloor eruptions at the East Pacific Rise, 9°50'N. *Geophysical Research Letters*, 49, e2021GL095459. <https://doi.org/10.1029/2021GL095459>

Received 27 JUL 2021

Accepted 19 JAN 2022

Author Contributions:

Conceptualization: T. Barreyre, R. Parnell-Turner, D. J. Fornari
Data curation: T. Barreyre, R. Parnell-Turner, J.-N. Wu, D. J. Fornari
Methodology: T. Barreyre
Writing – original draft: T. Barreyre
Writing – review & editing: T. Barreyre, R. Parnell-Turner, D. J. Fornari

Abstract Permeability controls energy and matter fluxes in deep-sea hydrothermal systems fueling a 'deep biosphere' of microorganisms. Here, we indirectly measure changes in sub-seafloor crustal permeability, based on the tidal response of high-temperature hydrothermal vents at the East Pacific Rise 9°50'N preceding the last phase of volcanic eruptions during 2005–2006. Ten months before the last phase of the eruptions, permeability decreased, first rapidly, and then steadily as the stress built up, until hydrothermal flow stopped altogether ~2 weeks prior to the January 2006 eruption phase. This trend was interrupted by abrupt permeability increases, attributable to dike injection during last phase of the eruptions, which released crustal stress, allowing hydrothermal flow to resume. These observations and models suggest that abrupt changes in crustal permeability caused by magmatic intrusion and volcanic eruption can control first-order hydrothermal circulation processes. This methodology has the potential to aid eruption forecasting along the global mid-ocean ridge network.

Plain Language Summary Permeability governs how fluids such as water and melt flow beneath the seafloor, and is influenced by diverse magmatic, volcanic, and tectonic forces as new oceanic crust is formed and altered over time. Despite being a master variable controlling the fluxes of energy and matter in deep-sea hydrothermal systems, permeability remains a poorly constrained hydrologic parameter of the oceanic crust. Here, we indirectly measure changes in crustal permeability for the first time, using the tidal response of high-temperature hydrothermal vents on the East Pacific Rise at 9°50'N preceding the last phase of volcanic eruptions in 2005–2006. We show that abrupt changes in crustal permeability caused by magmatic intrusion and volcanic eruption can control first-order hydrothermal circulation processes.

1. Introduction

Since their discovery in 1979 (Spiess et al., 1980), high-temperature 'black-smoker' hydrothermal vents along mid-ocean ridges (MORs) have been recognized as key components of Earth-ocean chemical and heat-exchange phenomena. MOR hydrothermal venting contributes to Earth's internal heat loss (e.g., Stein & Stein, 1994) and global ocean chemical budgets (e.g., Elderfield & Schultz, 1996). It is also essential to chemosynthetic processes that sustain biogeochemical cycles within hydrothermal vent communities (e.g., Kelley et al., 2002), which are considered likely modern analogs for early lifeforms on Earth and potential life elsewhere in our solar system (e.g., Waite et al., 2017). Sub-seafloor hydrothermal processes also significantly alter the composition of the oceanic crust (e.g., Elderfield & Schultz, 1996), control the thermo-mechanical and hydration states of newly formed oceanic lithosphere (e.g., German & Lin, 2004), and contribute to the generation of massive ore and hydrate deposits both on and below the seabed (e.g., Jamieson & Gartman, 2020).

The impacts of hydrothermal fluid circulation on each of the above processes or systems are directly linked to the magnitude and variability of the volume, heat, and chemical fluxes exiting the seafloor, which are all intrinsically controlled by the permeability of the seafloor. Yet despite its importance, permeability remains the most poorly constrained hydrologic parameter for oceanic crust (Wilcock & Fisher, 2004). Vent fluid temperature time-series data can provide a first-order indication and proxy record of hydrothermal system behavior over years to decades (e.g., Barreyre, Escartín, Sohn, Cannat, Ballu, & Crawford, 2014; Fornari, Shank, et al., 1998; Scheirer et al., 2006). In turn, these data can be used to infer temporal changes in permeability of the oceanic crust beneath the MOR crest (Barreyre & Sohn, 2016), and how they are impacted by tectonic and magmatic events (e.g.,

© 2022 The Authors.

This is an open access article under the terms of the [Creative Commons Attribution-NonCommercial License](https://creativecommons.org/licenses/by/4.0/), which permits use, distribution and reproduction in any medium, provided the original work is properly cited and is not used for commercial purposes.

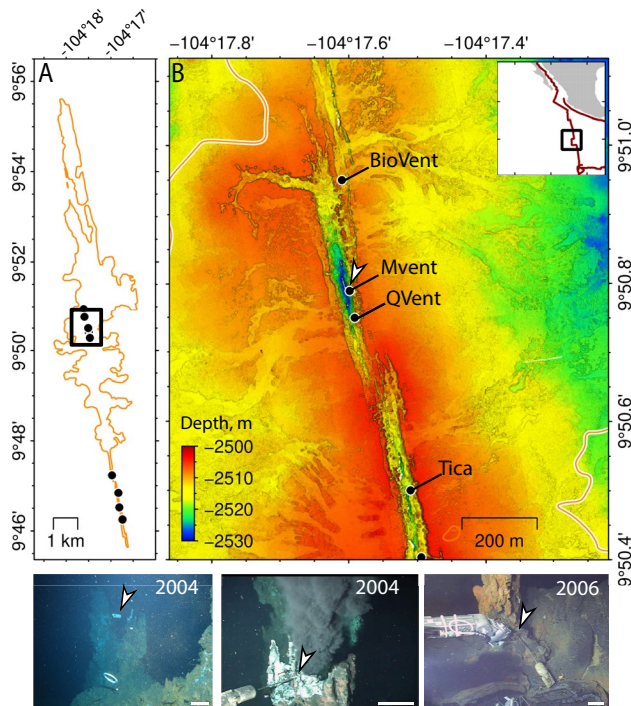


Figure 1. (a) High-temperature hydrothermal vents (black dots) and extent of the 2005–2006 EPR 9°50'N eruptions extent (orange outline; Soule et al., 2007). (b) Near-bottom bathymetry (Wu et al., 2022), and hydrothermal vents (labeled); white arrow shows location of photographs at M-vent (lower panel). Inset: black box shows study site and plate boundaries (red lines). Lower panels: Photographs (taken during *Alvin* dives) of the high-temperature logger (white arrowhead) deployed at M-vent in 2004 (left and center) and recovered in June 2006 (right). Note that the sensor was fully inserted into the vent orifice in 2004 (center); and recovered in 2006 still cemented into the side of the chimney with the 2005–2006 lava flow surface ~ 10 cm below sensor. White bars in photographs are ~ 25 cm.

Dziak et al., 2003; Johnson et al., 2000; Nooner & Chadwick, 2016; Sohn et al., 1998; Tolstoy et al., 2006; Wilcock et al., 2016).

Although numerous high-temperature vent fluids have been sampled along the global MOR (e.g., Fornari & Embley, 1995; Humphris & Klein, 2018), the geometry, permeability and longevity of hydrologic pathways within the upper oceanic crust, and their interactions with the underlying magmatic system, remain enigmatic (Butterfield et al., 1997; Von Damm, 2000; Wilcock & Fisher, 2004). Here we report on ~ 20 -month-long, *in situ* vent fluid temperature records from two deep-sea hydrothermal vents at the EPR near 9°50'N (Figure 1). The vent fluid temperature variations and modeled up-flow zone permeability estimates document, for the first time, the dynamic interactions and impacts of magmatic intrusion and volcanic eruptions on MOR hydrothermal processes.

2. Geological Setting and Monitoring Experiment

Numerous hydrothermal vent sites along the EPR axis between 9–10°N have been mapped (Haymon et al., 1991) and sampled since their discovery in 1989 (Fornari et al., 2012; Haymon et al., 1993; Von Damm et al., 1995; Figure 1a). All EPR high-temperature vents documented to date between 9°46'–51'N are located within the ~ 40 – 100 m-wide axial summit trough [AST; Escartín et al., 2007; Fornari, Haymon et al., 1998; Fornari, et al., 2004; Soule et al., 2007]. Focused hydrothermal circulation within the AST is thought to be driven by repeated diking events located beneath or immediately proximal to the AST (Fornari et al., 2004). Melt is sourced from a nearly continuous, ~ 50 – 100 m-thick axial magma lens, located ~ 1.5 km below the axis (Carbotte et al., 2013; Marjanović et al., 2018), that is heating fluids in a reaction zone above the magma body (Foustoukos & Seyfried, 2007).

Nine self-recording vent fluid temperature loggers were deployed at vents in the 9°46'–51'N study area in 2004, however, only two instruments survived the volcanic eruptions in 2005–2006. M-vent, located within the axis of the EPR at 9°50.6'N (Figure 1b), provides the most continuous record of vent temperature behavior pre- and post-eruption from April 2004 to late February 2006 (Figure 2a and Figure S1b in Supporting Information S1).

3. Sensor Description

The Multidisciplinary Instrumentation in Support of Oceanography (MISO) high-temperature vent fluid loggers used for this study contained two Onset Computer™ (<https://www.onsetcomp.com/>) temperature recording chips connected to resistance temperature device (RTD) sensors, each with a resolution of 1°C. The sensing capability of this instrument was limited to the range between 152 and 408°C because they are 8-bit devices (see Fornari, Shank, et al., 1998 for instrument details). Exit-vent fluid temperatures were recorded continuously over >20 months at 36 min intervals (Figures S1 and S2 in Supporting Information S1).

4. Exit-Fluid Thermal Response

Prior to the eruptions, M-vent was observed and sampled in April 2004 using the submersible *Alvin*. At that time, a temperature logger was installed in a chimney that was vigorously venting fluids at ~ 365 °C (Figures 2a and 3a). The uniformly high vent temperatures at M-vent prior to subsequent *Alvin* dives in November 2004 imply a stable plumbing system and hydrothermal source. The logger was disturbed by *Alvin* sampling vent fluids in November 2004 and March 2005, causing two small anomalies in the time-series record at those times (Figure 2a). After March 2005, no *Alvin* (or other known submersible) operations occurred at this vent that could have disrupted the time-series temperature record. There are, however, four prominent anomalies in the M-vent data that may be

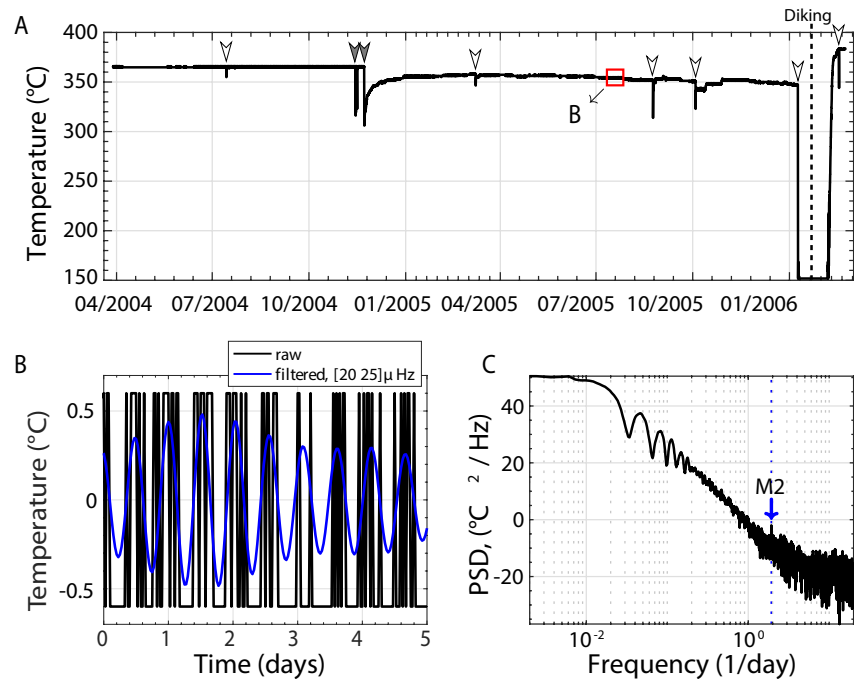


Figure 2. (a) Temperature record at M-vent for the period from April 2004 to February 2006 (data file VonDamm_M_623731_alv3993_2004). Gray-filled arrowheads are temperature anomalies caused by *Alvin* operations; white arrowheads are naturally-occurring anomalies; red box shows portion of the time series enlarged in (b). (b): Example of the tidal signature in the unfiltered (black) and filtered (blue) temperature signals, over a 5-day time window in the high-temperature data recorded at M-vent shown in (a). Note that we provide a filtered version of the signal to assist in viewing the tidal signature; but we do not use the filtered signal in any of the analysis nor modeling discussed in the paper, only the raw data are used. (c): Corresponding power spectrum (PSD) for the entire unfiltered temperature time series at M-vent shown in (a). Spectral analysis was performed by using the multi-taper method described in Section 6. The frequency of the main semidiurnal tidal harmonic M2 is shown as blue dashed line. Note that the M2 frequency peak is clearly visible and shown by blue arrow.

linked to magmatic perturbations of the hydrothermal system feeding this vent (Figures 2a and 3a and S1b in Supporting Information S1). Two relatively short duration (~1–3 days) events in August and October 2005 produced sudden ~50°C decreases in vent temperature. The last two anomalies in January and February 2006 captured the final phase of the 2005–2006 volcanic eruptions, which profoundly disrupted the M-vent hydrothermal system (Figures 2a and 3a and S1 in Supporting Information S1).

During less than 3 hr on January 9, 2006, M-vent exit fluid temperatures dropped from ~350°C to below 152°C (i.e., the lower threshold of the temperature logger measurement range). This event occurred ~13 days before an episode of microseismicity that has been linked with one phase of diking and volcanism at the study site on January 22, 2006 (Figures 2a and 3a and S1b in Supporting Information S1, vertical dashed line; Tolstoy et al., 2006). On February 6, 2006, the temperature rose abruptly above 152°C, reaching 376°C in 6 days. The temperature response was erratic for the first 2 days in this interval, then monotonically increased for the next 4 days, and finally plateaued at ~376°C on February 12, 2006. For the next 10 days, the temperature was relatively steady with small increases, finally reaching a stable temperature of ~384°C on February 18, 2006 (~25 days after the microseismic episode). The stable exit-fluid temperature, after the eruption-induced perturbations, was ~30°C above the pre-eruption vent fluid temperatures. On February 23, 2006, the M-vent record stopped due to low battery power.

The M-vent logger was sighted in May 2006 during a towed camera survey that initially mapped and sampled flows emplaced during the 2005–2006 eruptions (Cowen et al., 2007, Figures 1 and S2 in Supporting Information S1). In late June 2006, M-vent appeared to be inactive, however seafloor photographs in May of 2006 revealed white microbial staining on the chimney and surrounding basalt surface, consistent with the eruption or enhanced hydrothermal activity occurring months before (Cowen et al., 2007). The M-vent logger was recovered by *Alvin* on June 26, 2006 (~150 days after the January 2006 phase of the eruptions), when the vent was

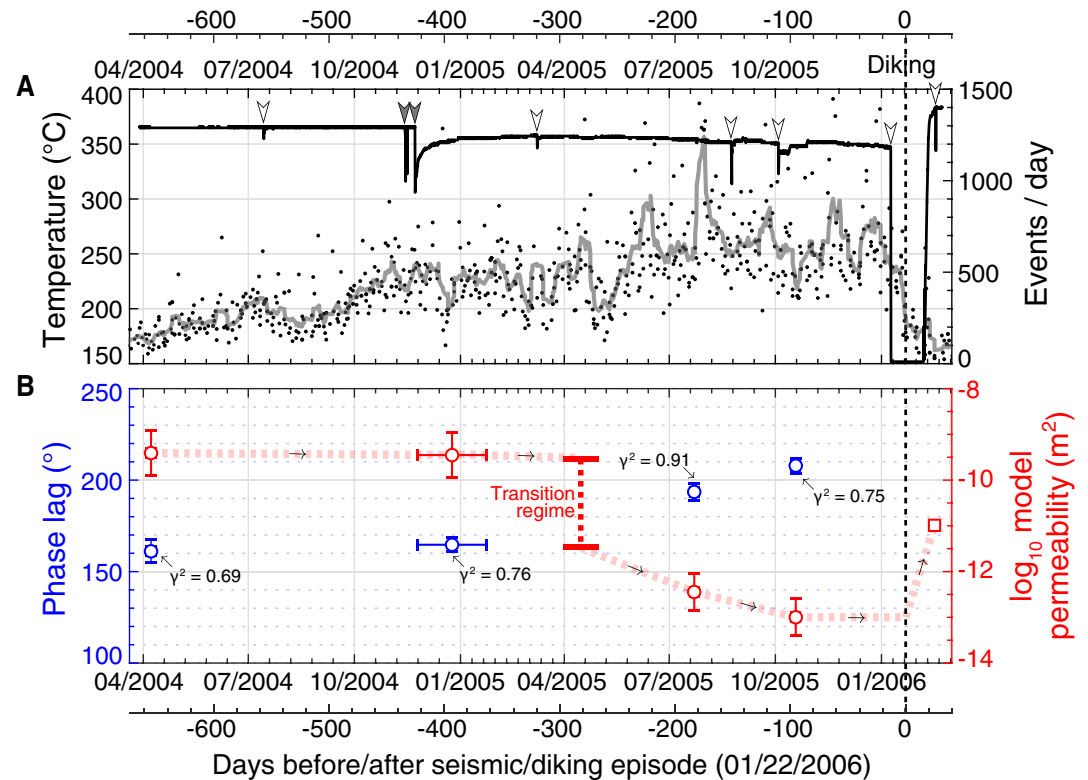


Figure 3. Temperature, seismicity, phase lag, and permeability at M-Vent for the period from April 2004 to February 2006. (a) Vent fluid temperature (black line) and seismicity (dots); gray line shows running average of earthquake rate (Tolstoy et al., 2006). Gray arrowheads are temperature drops caused by *Alvin* operations. White arrowheads are naturally-occurring anomalies in the exit-fluid temperature behavior. (b) Blue circles are phase lag between tidal loading and temperature at M2 period; highest coherency (r^2) phase lag estimates for each time cluster are shown (160°, 165°, 190°, 210°), details of error estimates provided in Section 6. Red circles are permeability from phase lag estimates (details of error estimates in Section 7.1); vertical, bold dashed red line shows inferred change from high- to low-permeability poroelastic regimes; horizontal, light dashed red lines show speculative evolution of permeability through time; red square is post-eruption permeability estimate (see Section 7.2).

confirmed to be inactive. The 2006-erupted lava was observed to have engulfed the lower portion of the M-vent chimney to a level that reached ~50 cm below where the logger was cemented into the side of the chimney wall and was ~10 cm below the logger housing (Figures 1 and S2 in Supporting Information S1).

Continuous temperature data were also recorded at Q-vent, located ~100 m south of M-vent (Figure 1), from 2004 to late 2005. The logger at Q-vent was also recovered in June 2006, and recorded vent-fluid temperatures that steadily increased from 342°C in late March 2004 to 352°C in December 2005 (Figures S1C in Supporting Information S1). Despite being located only ~100 m south of M-vent, no fluid temperature anomalies are observed in the Q-vent time-series temperature data; the recording stopped because of low power before the January 2006 event recorded at M-vent. The Q-vent logger was recovered by *Alvin* from a 320°C actively venting chimney in June 2006, a decrease of over 30°C in fluid temperature from the highest pre-eruption value.

5. Physical Explanation

We used the vent temperature response to tidal forcing at M- and Q-vents to constrain the subsurface permeability of the fluid pathway, which lies between the seafloor and the top of the magma lens (~1,500 m below seafloor; Carbotte et al., 2013; Marjanović et al., 2018). We used these measurements to infer the phase lag between vent temperatures and tides, and hence permeability variations inside the crustal up-flow zone from ~April 2004 to January 2006 (Barreyre & Sohn, 2016; Barreyre et al., 2018). The temperature records and power spectra show clear tidal oscillations imposed upon the average vent discharge temperature, with a maximum energy peak at the lunar semidiurnal (M2) tide frequency (Figure 2).

Ocean tidal oscillations exert an external load on oceanic-crust hosted hydrothermal systems. The resulting stress is exerted partly by the solid matrix and partly by the interstitial fluid, where it manifests as a change in fluid pressure, or a pore pressure perturbation. Tidal forcing imposes an instantaneous pressure perturbation with a constant magnitude at all depths and a time-dependent pore pressure perturbation resulting from flow-induced diffusion (Van der Kamp & Gale, 1983). The instantaneous signal is in-phase with the ocean tide, while the diffusive pressure perturbation cyclically modifies pore pressures and the upwelling fluid velocity at the forcing periods. These perturbations result in a phase lag between the temperature (our proxy for vertical fluid velocity), and the tidal loading function, which depends upon the poroelastic parameters (i.e., permeability) of the system (Barreyre, Escartín, Sohn, & Cannat, 2014; Barreyre et al., 2018; Crone & Wilcock, 2005; Jupp & Schultz, 2004). The poroelastic response is highly sensitive to matrix permeability, which controls the diffusion rate of pore pressure perturbations, as well as the velocity of the hydrothermal fluids. To a first order, phase lag is inversely related to permeability (Barreyre et al., 2018). Using tidal response to measure hydrogeologic properties has two distinct advantages. First, tidal response is passive, and records the *in situ* properties undisturbed by local (vent-scale) temperature changes or mixing with seawater. Second, tidal response provides a continuous temporal record of hydrogeologic properties in the matrix hosting the hydrothermal flow.

6. Phase Lag Estimates

The time series and respective power spectra of the temperature records show clear tidal oscillations superimposed on the long-term trend (Figure 2). We estimated the coherency and phase lag between tidal pressure at the seafloor (data generated with the GOT4.7 global ocean tide model of Ray (2013) as described in Barreyre & Sohn, 2016; Figure S1A in Supporting Information S1), and raw exit-fluid temperature time series, which were analyzed by applying multitaper cross-spectral methods with adaptive weighting to sliding time windows (Efron & Stein, 1981; Percival & Walden, 1993; Thomson, 1982). We used a range of time windows (8, 15, 30 and 60 days), and time-half bandwidth products ($NW = 3.5$ and 4) to maximize the signal-to-noise ratio and thus estimate the highest coherence at the M2 frequency between temperature and pressure with the smallest errors on both the estimated coherence and associated phase lags (Figure S3 in Supporting Information S1). Phase lag uncertainties are estimated by resampling (i.e., jackknifing; Tukey, 1958) the independent Fourier coefficients obtained for the set of orthogonal tapers generated by the multitaper method (Barreyre & Sohn, 2016). Variability in the coherency is caused by noise in the exit-fluid temperature data and relatively low resolution of the sensors. To minimize the impact of this variability and maximize the signal-to-noise ratio, we restricted our phase angle analysis to time windows with a coherency ($\gamma^2 \geq 0.6$) at the M2 frequency (colored boxes in Figure S3 in Supporting Information S1) and retained only the highest coherency values ($\gamma^2 \geq 0.7$) for each time cluster (black dots in Figure S3B in Supporting Information S1) for poroelastic modeling. For multiple data records acquired contemporaneously in the same housing (as is common in many deployments: Barreyre, Escartín, Sohn, Cannat, Ballu, & Crawford, 2014; Fornari, Shank, et al., 1998), we only used the record with the highest coherency to tidal pressure at the M2 frequency.

7. Permeability Estimates

7.1. Poroelasticity

Following the methodology described by Barreyre, Escartín, Sohn, and Cannat (2014) and Barreyre and Sohn (2016), we use highly coherent ($\gamma^2 \geq 0.7$) phase lags in conjunction with the analytical model of Jupp and Schultz (2004) and Barreyre et al. (2018) to constrain poroelastic parameters (e.g., permeability) at the M- and Q-vent sites from April 2004 to February 2006. For consistency, we use the same baseline modeling parameters (i.e., storage compressibility, porosity, bulk density, grain bulk modulus, fluid bulk modulus, and matrix- drained- modulus) as Crone and Wilcock (2005) and Barreyre et al. (2018), and references therein. We initialize the model with a homogeneous medium (i.e., single-layer) for two reasons: first, layer 2A (extrusive) is thin (~ 150 m) compared to layer 2B (intrusive) near $9^\circ 50' N$ on the EPR (1,500 m; Marjanović et al., 2018). Second, the intrinsic poroelastic parameters of each layer are poorly constrained (e.g., how they evolve in space and time when responding to additional stress is not well known), hence adopting a single-layer model simplifies the analysis to estimate first-order changes in permeability.

In a single-layer model, the depth of the boundary that arrests the downward propagation of the tidally induced pressure gradient (i.e., the thickness of the permeable layer, H) is a key parameter. For basalt-hosted vent fields the two primary lithologic interfaces where the permeability changes significantly are: (a) the extrusive/intrusive boundary (i.e., seismic layer 2A/2B), and (b) the intrusive/cumulate boundary (i.e., base of seismic layer 2B, equivalent to magma chamber depth). At the EPR 9°50'N study site, these interface depths have been constrained by seismic reflection experiments (Carbotte et al., 2013; Marjanović et al., 2018), which provide a template for our models. We do not know, *a priori*, the propagation depth for the tidal loading pressure signal, so the model was run with two different values for the permeable layer thickness, H , at each site: (a) H = depth to the layer 2A/2B interface and (b) H = depth to the axial magma lens. These different assumptions for H do not change the order of magnitude of the crustal up-flow zone permeability required to fit the phase lag data (Figure S4 in Supporting Information S1), and they provide comprehensive ranges for first-order permeability changes within the crustal plumbing system (i.e., error bars on Figure 3b).

7.2. Darcy Equation

Because we have no phase lag estimates post-eruption to constrain the permeability, we instead use the Darcy equation constrained by our observations. We first estimated the mean flow velocity u from the distance between the top of the magma chamber (reaction zone) and the seafloor (1,500 m), and the time it took for fluids to travel that distance after flow was resumed after the diking event on January 22, 2006 (~25 days). We obtain a mean flow velocity of $\sim 7 \times 10^{-4} \text{ m s}^{-1}$. For a permeable, homogeneous crust and assuming that both density and dynamic viscosity do not vary with depth (Jupp & Schultz, 2004), the buoyancy-driven vertical Darcy velocity, u , can be defined by

$$u = \frac{gk(\rho_0 - \rho_f)}{\mu}$$

where $g = 9.8 \text{ m s}^{-2}$ is gravitational acceleration, k is permeability (m^2), $\rho_0 = 1,015.6 \text{ kg m}^{-3}$ and $\rho_f = 553.8 \text{ kg m}^{-3}$ are the densities of seawater (calculated with $T_0 = 2^\circ\text{C}$ at 32.5 MPa) and hot hydrothermal fluid (calculated with $T_f = 380^\circ\text{C}$ at 32.5 MPa), respectively, and $\mu = 6.4 \times 10^{-5} \text{ Pa s}$ is the dynamic viscosity. Rearranging, we estimate permeability k to be $\sim 10^{-11.0064} \text{ m}^2$ (see Figure 2b).

8. Results and Discussion

8.1. Permeability Changes

We translated the estimated phase responses into permeability values based on analytical solutions for a one-dimensional homogeneous poroelastic model of a hydrothermal system (Barreyre, Escartín, Sohn, & Cannat, 2014; Barreyre et al., 2018; Jupp & Schultz, 2004; Figure S4 in Supporting Information S1). At M-vent, the estimated phase lag values remain uniform at $\sim 160^\circ$ – 165° from \sim April 2004 to January 2005, and then steadily increased by 50° during ~ 1 year to $\sim 210^\circ$, prior to the seismic/diking event on January 22, 2006. The corresponding permeability varied by < 4 orders of magnitude (from $10^{-9.5} \text{ m}^2$ to 10^{-13} m^2) over the year preceding this diking event (Figure 3b).

8.2. Stress Changes

Based on the work of Pollard and Segall (1987) and Wilcock et al. (2009), who describe stress perturbations resulting from emplacement of pressurized magma forming a thin sill within oceanic crust, we suggest that such stress changes are associated with inflation of the AML. The intrusion of dikes feeding seafloor volcanic eruptions results in permeability changes that, in turn, affect the hydrothermal flow. In the case of the EPR axis at M- and Q-vents, we propose that subsurface magmatic activity started in spring 2005, well before the eruption event on January 22, 2006. These early magmatic phases caused stress perturbations resulting from the progressive injection of magma into a sill, which —while inducing horizontal deviatoric extension— made both the vertical and horizontal total stresses more compressive directly above the AML (Olive & Dublanche, 2020; Pollard & Segall, 1987). This stress-state could have exerted excess pressure on pre-existing pores and cracks throughout the reaction zone and along fluid pathways (Figure 4), resulting in a decrease in permeability within M- and Q-

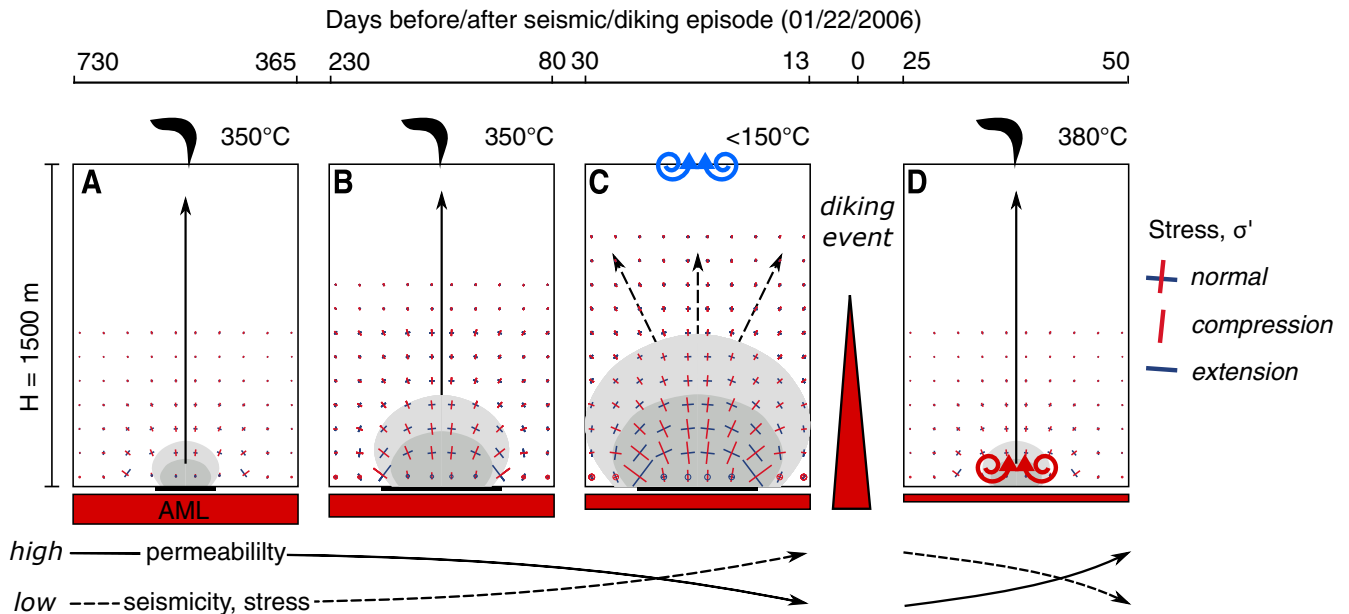


Figure 4. Conceptual across-axis cross-sections above axial magma lens (AML) showing changes in crustal deviatoric stress and permeability experienced by a high-temperature hydrothermal vent before, during and after a volcanic eruption. Schematic deviatoric stress perturbations are displayed above one side of a pressurized horizontal crack (bold black line) showing maximum compressional and extensional normal stress perturbations, red and blue lines, respectively, and maximum shear stresses (shaded areas), from Wilcock et al. (2009). The stress perturbations, while inducing horizontal deviatoric extension, made both the vertical and horizontal total stresses more compressive directly above the AML (Pollard & Segall, 1987). (a–c): Stress builds up before eruption, resulting in a decrease in permeability within the hydrothermal plumbing system (and hence in flow velocity), until the final eruption phase in January 2006 where hydrothermal flow was disrupted 13 days before main seismic/diking event on January 22, 2006. (d) Diking occurs and stress released: increased permeability results in recovery of hydrothermal flow at a higher temperature with additional heat from dike injection.

vents' plumbing systems. The abrupt change in poroelastic regimes in April–May 2005, from a high- to low-permeability regime (“transition regime” in Figures 3b and S4 in Supporting Information S1) reflects non-linear behavior of the stress-permeability coupling. This regime change also corresponds to changes in slope and scatter of the average daily seismic event rate (Tolstoy et al., 2006; Figure 3a).

The decrease in permeability of ~four orders of magnitude likely caused the Darcy upward velocity of the hydrothermal fluids to decrease by the same amount. This decrease resulted in significant disruption of the hydrothermal flow ~13 days before the diking event. The reduction (and possible cessation) of hydrothermal fluid flow led to a change in the mixing ratio with relatively more cold seawater and hence a drastic drop of vent temperature (dropping below 152°C, the lower sensitivity limit of the logger). On January 22, 2006, the diking event occurred and was associated with a drop in the microseismicity, relieving the crustal stress imposed by the inflating AML and increasing the permeability in the up-flow zone. The post-eruptive stress change restored the hydrothermal flow after a few weeks, resulting in significantly higher exit-fluid temperature, enhanced by the additional heat from the dike that fed the final phase of the 2005–2006 seafloor eruptions in the 9°50'N area.

9. Conclusions

Our study provides a new view of the underlying dynamic coupling between hydrothermal systems and associated seafloor spreading phenomena. We have tracked crustal permeability before, during, and after volcanic eruptions, using the phase lag between tide and hydrothermal vent temperature. We find that hydrothermal flow ceased 2 weeks before the final eruption phase, and that diking events can be directly linked to changes in permeability. Both data and models indicate that permeability and fluid flow in this dynamic environment were disrupted rapidly at the onset and during this final phase of the 2005–2006 eruptions.

The field and analytical methods used in this study could allow researchers to constrain the permeability structure, energy fluxes and variability of hydrothermal fluids elsewhere along the global MOR by acquiring multi-year exit-fluid temperature time-series data from high-temperature hydrothermal vents. These results demonstrate a

practical approach for tracking and modeling the magmatic inflation of sub-ridge axial magma reservoirs and ensuing volcanic eruptions, determining the impacts of these seafloor spreading processes on hydrothermal systems, and ultimately expanding the potential of forecasting seafloor eruptions along the global MOR.

Conflict of Interest

The authors declare no conflicts of interest relevant to this study.

Data Availability Statement

Data used in this study can be found at Marine Geoscience Data System (MGDS - <https://doi.org/10.26022/IEDA/330422> - <https://www.marine-geo.org/tools/files/30422>).

Acknowledgments

This research is funded by National Science Foundation (NSF) grants to D. J. Fornari and T. Barreyre (OCE-1949485), and to R. Parnell-Turner (OCE-1948936). T. Barreyre was supported by the University of Bergen, Norway. The authors are grateful to William Chadwick and Daniela Di Iorio for detailed and constructive reviews that significantly improved the manuscript, and to Editor Christian Huber. We dedicate this paper to Karen Von Damm.

References

- Barreyre, T., Escartin, J., Sohn, R., & Cannat, M. (2014). Permeability of the Lucky Strike deep-sea hydrothermal system: Constraints from the poroelastic response to ocean tidal loading. *Earth and Planetary Science Letters*, *408*, 146–154. <https://doi.org/10.1016/j.epsl.2014.09.049>
- Barreyre, T., Escartin, J., Sohn, R. A., Cannat, M., Ballu, V., & Crawford, W. C. (2014). Temporal variability and tidal modulation of hydrothermal exit-fluid temperatures at the Lucky Strike deep-sea vent field, Mid-Atlantic Ridge. *Journal of Geophysical Research: Solid Earth*, *119*(4), 2543–2566. <https://doi.org/10.1002/2013jb010478>
- Barreyre, T., Olive, J. A., Crone, T. J., & Sohn, R. A. (2018). Depth-dependent permeability and heat output at basalt-hosted hydrothermal systems across mid-ocean ridge spreading rates. *Geochemistry, Geophysics, Geosystems*, *19*, 1259–1281. <https://doi.org/10.1002/2017gc007152>
- Barreyre, T., & Sohn, R. A. (2016). Poroelastic response of mid-ocean ridge hydrothermal systems to ocean tidal loading: Implications for shallow permeability structure. *Geophysical Research Letters*, *43*, 1660–1668. <https://doi.org/10.1002/2015gl066479>
- Butterfield, D. A., Jonasson, I. R., Massoth, G. J., Feely, R. A., Roe, K. K., Embley, R. W., et al. (1997). Seafloor eruptions and evolution of hydrothermal fluid chemistry. *Philosophical Transactions of the Royal Society of London - A*, *355*, 369–386. <https://doi.org/10.1098/rsta.1997.0013>
- Carbotte, S., Marjanović, M., Carton, H., Mutter, J. C., Canales, J. P., Nedimović, M. R. et al. (2013). Fine-scale segmentation of the crustal magma reservoir beneath the East Pacific Rise. *Nature Geoscience*, *6*, 866–870. <https://doi.org/10.1038/ngeo1933>
- Cowen, J. P., Glazer, B., Fornari, D. J., Shank, T. M., Soule, S. A., Love, B., et al. (2007). Volcanic eruptions at East Pacific rise near 9°50' N. *Eos Transactions American Geophysical Union*, *88*(7), 81–83. <https://doi.org/10.1029/2007eo070001>
- Crone, T. J., & Wilcock, W. S. D. (2005). Modeling the effects of tidal loading on mid-ocean ridge hydrothermal systems. *Geochemistry, Geophysics, Geosystems*, *6*(7), Q07001. <https://doi.org/10.1029/2004gc000905>
- Dziak, R. P., Chadwick, W. W., Jr, Fox, C. G., & Embley, R. W. (2003). Hydrothermal temperature changes at the southern Juan de Fuca Ridge associated with MW 6.2 Blanco transform earthquake. *Geology*, *31*, 119–122. [https://doi.org/10.1130/0091-7613\(2003\)031<0119:htcats>2.0.co;2](https://doi.org/10.1130/0091-7613(2003)031<0119:htcats>2.0.co;2)
- Efron, B., & Stein, C. (1981). The jackknife estimate of variance. *Annals of Statistics*, 586–596. <https://doi.org/10.1214/aos/1176345462>
- Elderfield, H., & Schultz, A. (1996). Mid-ocean ridge hydrothermal fluxes and the chemical composition of the ocean. *Annual Review of Earth and Planetary Sciences*, *24*, 191–224. <https://doi.org/10.1146/annurev.earth.24.1.191>
- Escartin, J., Soule, S. A., Fornari, D. J., Tivey, M. A., Schouten, H., & Perfit, M. R. (2007). Interplay between faults and lava flows in construction of the upper oceanic crust: The East Pacific Rise crest 9°25'–9°58' N. *Geochemistry, Geophysics, Geosystems*, *8*(6), Q06005. <https://doi.org/10.1029/2006GC003199>
- Fornari, D. J., & Embley, R. W. (1995). Tectonic and volcanic controls on hydrothermal processes at the mid-ocean ridge: An overview based on near-bottom and submersible studies. *Seafloor hydrothermal systems: Physical, chemical, biological, and geological interactions*, *91*, 1–46.
- Fornari, D. J., Haymon, R. M., Perfit, M. R., Gregg, T. K. P., & Edwards, M. H. (1998). Geological characteristics and evolution of the axial zone on fast spreading mid-ocean ridges: Formation of an axial summit Caldera along the East Pacific Rise, 9°–10°N. *Journal of Geophysical Research*, *103*, 9827–9855. <https://doi.org/10.1029/98jb00028>
- Fornari, D. J., Shank, T., Von Damm, K. L., Gregg, T. K. P., Lilley, M., Bray, A., et al. (1998). Time-series temperature measurements at high-temperature hydrothermal vents, East Pacific Rise 9°49'–51' N: Evidence for monitoring a crustal cracking event. *Earth and Planetary Science Letters*, *160*, 419–431. [https://doi.org/10.1016/s0012-821x\(98\)00101-0](https://doi.org/10.1016/s0012-821x(98)00101-0)
- Fornari, D. J., Tivey, M., Schouten, H., Perfit, M., Yoerger, D., Bradley, A., et al. (2004). Submarine lava flow emplacement at the East Pacific Rise 9°50' N: Implications for uppermost ocean crust stratigraphy and hydrothermal fluid circulation. *Mid-Ocean Ridges: Hydrothermal Interactions Between the Lithosphere and Oceans. Geophysical Monograph Series*, *148*, 187–218. <https://doi.org/10.1029/148GM08>
- Fornari, D. J., Von Damm, K. L., Bryce, J. G., Cowen, J. P., Ferrini, V., Fundis, A., et al. (2012). The East Pacific Rise between 9°N and 10°N: Twenty-five years of integrated, multidisciplinary oceanic spreading center studies. *Oceanography*, *25*, 18–43. <https://doi.org/10.5670/oceanog.2012.02>
- Foustoukos, D. I., & Seyfried, W. E., Jr. (2007). Quartz solubility in the two-phase and critical region of the NaCl–KCl–H₂O system: Implications for submarine hydrothermal vent systems at 9°50' N East Pacific Rise. *Geochimica et Cosmochimica Acta*, *71*, 186–201. <https://doi.org/10.1016/j.gca.2006.08.038>
- German, C. R., & Lin, J. (2004). The thermal structure of the oceanic crust, ridge-spreading and hydrothermal circulation: How well do we understand their inter-connections. *Mid-ocean ridges: hydrothermal interactions between the lithosphere and oceans, Geophysical Monograph Series*, *148*, 1–18. <https://doi.org/10.1029/148GM01>
- Haymon, R. M., Fornari, D. J., Edwards, M. H., Carbotte, S., Wright, D., & Macdonald, K. C. (1991). Hydrothermal vent distribution along the East Pacific Rise crest (9°09'–54' N) and its relationship to magmatic and tectonic processes on fast-spreading mid-ocean ridges. *Earth and Planetary Science Letters*, *104*, 513–534. [https://doi.org/10.1016/0012-821x\(91\)90226-8](https://doi.org/10.1016/0012-821x(91)90226-8)
- Haymon, R. M., Fornari, D. J., Von Damm, K. L., Lilley, M. D., Perfit, M. R., Edmond, J. M., et al. (1993). Volcanic eruption of the mid-ocean ridge along the East Pacific Rise crest at 9°45'–52' N: Direct submersible observations of seafloor phenomena associated with an eruption event in April, 1991. *Earth and Planetary Science Letters*, *119*(1–2), 85–101. [https://doi.org/10.1016/0012-821x\(93\)90008-w](https://doi.org/10.1016/0012-821x(93)90008-w)

- Humphris, S. E., & Klein, F. (2018). Progress in deciphering the controls on the geochemistry of fluids in seafloor hydrothermal systems. *Annual Review of Marine Science*, 10, 315–343. <https://doi.org/10.1146/annurev-marine-121916-063233>
- Jamieson, J. W., & Gartman, A. (2020). Defining active, inactive, and extinct seafloor massive sulfide deposits. *Marine Policy*, 117, 103926. <https://doi.org/10.1016/j.marpol.2020.103926>
- Johnson, P. H., Hutnak, M., Dziak, R. P., Fox, C. G., Urcuyo, I., Cowen, J. P., et al. (2000). Earthquake-induced changes in a hydrothermal system on the Juan de Fuca mid-ocean ridge. *Nature*, 407, 174–177. <https://doi.org/10.1038/35025040>
- Jupp, T. E., & Schultz, A. (2004). A poroelastic model for the tidal modulation of seafloor hydrothermal systems. *Journal of Geophysical Research*, 109, B03105. <https://doi.org/10.1029/2003jb002583>
- Kelley, D. S., Baross, J. A., & Delaney, J. R. (2002). Volcanoes, fluids, and life at mid-ocean ridge spreading centers. *Annual Review of Earth and Planetary Sciences*, 30, 385–491. <https://doi.org/10.1146/annurev.earth.30.091201.141331>
- Marjanović, M., Carbotte, S. M., Carton, H. D., Nedimović, M. R., Canales, J. P., & Mutter, J. C. (2018). Crustal magmatic system beneath the East Pacific Rise (8°20' to 10°10' N): Implications for tectonomagmatic segmentation and crustal melt transport at fast-spreading ridges. *Geochemistry, Geophysics, Geosystems*, 19, 4584–4611. <https://doi.org/10.1029/2018GC007590>
- Nooner, S. L., & Chadwick, W. W. (2016). Inflation-predictable behavior and co-eruption deformation at Axial Seamount. *Science*, 354, 1399–1403. <https://doi.org/10.1126/science.aah4666>
- Olive, J. A., & Dublanche, P. (2020). Controls on the magmatic fraction of extension at mid-ocean ridges. *Earth and Planetary Science Letters*, 549, 116541. <https://doi.org/10.1016/j.epsl.2020.116541>
- Percival, D., & Walden, A. (1993). *Spectral analysis for physical applications*. Cambridge University Press.
- Pollard, D. D., & Segall, P. (1987). Theoretical displacements and stresses near fractures in rock: With applications to faults, joints, veins, dikes, and solution surfaces. In *Fracture mechanics of rock* (pp. 277–347). <https://doi.org/10.1016/b978-0-12-066266-1.50013-2>
- Ray, R. D. (2013). Precise comparisons of bottom-pressure and altimetric ocean tides. *Journal of Geophysical Research: Ocean*, 118, 4570–4584. <https://doi.org/10.1002/jgrc.20336>
- Scheirer, D. S., Fornari, D. J., & Shank, T. M. (2006). Temperature variations and diffuse and focused flow hydrothermal vent sites along the northern East Pacific Rise. *Geochemistry, Geophysics, Geosystems*, 7, Q03002. <https://doi.org/10.1029/2005GC001094>
- Sohn, R. A., Fornari, D. J., Von Damm, K. L., Hildebrand, J. A., & Webb, S. C. (1998). Seismic and hydrothermal evidence for a cracking event on the East Pacific Rise crest at 9°50' N. *Nature*, 396, 159–161. <https://doi.org/10.1038/24146>
- Soule, S. A., Fornari, D. J., Perfit, M. R., & Rubin, K. H. (2007). New insights into mid-ocean ridge volcanic processes from the 2005–2006 eruption of the East Pacific Rise, 9°46' N–9°56' N. *Geology*, 35, 1079–1082. <https://doi.org/10.1130/g23924a.1>
- Spiess, F. N., Macdonald, K. C., Atwater, T., Ballard, R., Carranza, A., Cordoba, D., et al. (1980). East Pacific rise: Hot springs and geophysical experiments. *Science*, 207, 1421–1433. <https://doi.org/10.1126/science.207.4438.1421>
- Stein, C. A., & Stein, S. (1994). Constraints on hydrothermal heat flux through the oceanic lithosphere from global heat flow. *Journal of Geophysical Research*, 99, 3081–3095. <https://doi.org/10.1029/93jb02222>
- Thomson, D. J. (1982). Spectrum estimation and harmonic analysis. *Proceedings of the IEEE*, 70(9), 1055–1096. <https://doi.org/10.1109/proc.1982.12433>
- Tolstoy, M., Cowen, J. P., Baker, E. T., Fornari, D. J., Rubin, K. H., Shank, T. M., et al. (2006). A sea-floor spreading event captured by seismometers. *Science*, 314, 1920–1922. <https://doi.org/10.1126/science.1133950>
- Tukey, J. (1958). Bias and confidence in not quite large samples. *The Annals of Mathematical Statistics*, 29, 614. <https://doi.org/10.1214/aoms/1177706635>
- Van der Kamp, G., & Gale, J. E. (1983). Theory of earth tide and barometric effects in porous formations with compressible grains. *Water Resources Research*, 19, 538–544. <https://doi.org/10.1029/wr019i002p00538>
- Von Damm, K. L. (2000). Chemistry of hydrothermal vent fluids from 9–10° N, East Pacific rise: “Time zero,” the immediate post-eruptive period. *Journal of Geophysical Research*, 105, 11203–11222. <https://doi.org/10.1029/1999jb900414>
- Von Damm, K. L., Oosting, S. E., Kozlowski, R., Buttermore, L. G., Colodner, D. C., Edmonds, H. N., et al. (1995). Evolution of East Pacific Rise hydrothermal vent fluids following a volcanic eruption. *Nature*, 375, 47–50. <https://doi.org/10.1038/375047a0>
- Waite, H. J., Glein, C. R., Perryman, R. S., Teolis, B. D., Magee, B. A., Miller, G., et al. (2017). Cassini finds molecular hydrogen in the enceladus plume: Evidence for hydrothermal processes. *Science*, 356, 155–159. <https://doi.org/10.1126/science.aai8703>
- Wilcock, W. S. D., & Fisher, A. T. (2004). Geophysical constraints on the sub-seafloor environment near mid-ocean ridges. *The Subseafloor Biosphere at Mid-Ocean Ridges, Geophysical Monograph Series*, 144, 51–74. <https://doi.org/10.1029/144gm05>
- Wilcock, W. S. D., Hooft, E. E. E., Toomey, D. R., McGill, P. R., Barclay, A. H., Stakes, D. S., & Ramirez, T. M. (2009). The role of magma injection in localizing black-smoker activity. *Nature Geoscience*, 2, 509–513. <https://doi.org/10.1038/ngeo550>
- Wilcock, W. S. D., Tolstoy, M., Waldhauser, F., Garcia, C., Tan, Y. J., Bohlenstiehl, D. R., et al. (2016). The 2015 eruption of Axial Seamount: Seismic constraints on caldera dynamics. *Science*, 354, 1395–1399. <https://doi.org/10.1126/science.aah5563>
- Wu, J.-N., Parnell-Turner, R., Fornari, D. J., Kurras, G., Berrios-Rivera, N., Barreyre, T., & McDermott, J. (2022). Extent and Volume of Lava Flows erupted at 9°50' N, East Pacific Rise in 2005–2006 from Autonomous Underwater Vehicle Surveys. *Geochemistry, Geophysics, Geosystems*. <https://doi.org/10.1029/2021gc010213>